Characterization of fast electron divergence and energy spectrum from modeling of angularly resolved bremsstrahlung measurements

T. S. Daykin[1,a)], H. Sawada[1,b)], Y. Sentoku[2], F. N. Beg[3],H. Chen[4], H. S. McLean[4], A. J. Link[4], P. K. Patel[4], and Y. Ping[4]
1. Department of Physics, University of Nevada Reno, Reno, NV, 89511, USA
2. Institute of Laser Engineering, Osaka University, Suita, Osaka, 565-0871, Japan
3. University of California San Diego, La Jolla, CA, 92093, USA
4. Lawrence Livermore National Laboratory, Livermore, CA, 94550, USA
a) tdaykin@unr.edu, b) hsawada@unr.edu

Characteristics of fast electrons generated in an intense laser-solid target interaction are studied by modeling angularly resolved bremsstrahlung measurements with a hybrid Particle-In-Cell (PIC) code, LSP. The experiment was performed using the 50 TW Leopard laser at the Nevada Terawatt Facility. A 100 μm thick Cu foil was irradiated by the 15 J, 0.35 ps laser at a peak laser intensity of 2×10^{19} W/cm^2. Bremsstrahlung produced by transport and recirculation of the fast electrons in the foil was measured with two differential filter-stack x-ray spectrometers at 22° and 40° from the laser axis. The two-spectrometer signals simultaneously fit by varying single slope temperatures (T_{hot}) and divergence angles (θ) enables for determining T_{hot} and θ to be 1.1 ± 0.3 MeV and 15° ± 8°, respectively. The T_{hot} inferred from the bremsstrahlung signals agrees with that from an escaped electron measurement, suggesting that that the bremsstrahlung is predominantly produced by the transport of the high energy fast electrons in the first pass.

1. Introduction

The interaction between an ultra-intense short-pulse laser and solid targets produces a substantial number of electrons with MeV energies. These relativistic electrons called fast or hot electrons are accelerated predominantly by the ponderomotive potential of the laser. Understanding of the physics of fast electron generation and transport is important for a number of applications such as generation of intense x-ray and gamma ray sources[1, 2], ion acceleration [3,4,5], neutron production[6], fast ignition (FI) fusion schemes [7,8], and medical applications[9]. Recently, bremsstrahlung produced by fast electrons has been applied for high energy broadband x-ray radiography of inertial confinement fusion plasma[10,11] and a millimeter diameter metal rod[12].

Laser-accelerated fast electrons can be characterized by three parameters: electron energy distribution, laser to electron conversion efficiency, and divergence angle of the electron beam. These properties have been extensively studied for the purpose of FI and a variety of x-ray and particle diagnostics for fast electron characterization have been developed[13]. It is still challenging to simultaneously determine the electron characteristics inside solid density targets because these parameters are closely correlated. In general, the higher the electron energy spectrum is, the narrower the divergence of the beam is. Both parameters are readily modified by collisions during the transport and sheath potentials developed on the surfaces confining the electrons around the target.

Bremsstrahlung X rays generated by the transport of the fast electrons carry information about the electrons inside the target and can be measured without modification of the signal by the sheath fields.[14,15,16,17,18,19,20,21,22] Bremsstrahlung spectrometers designed for short-pulse laser experiments usually consist of either differential metal filters that cover the photon energy ranges from ~ 10 keV to 800 keV[23,24] or high-Z filter arrays for the photon energies up to 2.5 MeV[17,25]. The recorded signals are modeled with Monte Carlo or hybrid Particle-in-cell (PIC) codes to match at each energy bin by varying input fast electron parameters.

Chen et al[26] and Westover et al[27] performed a series of Monte Carlo calculations to find a range of conversion efficiency and slope temperature assuming a fixed divergence angle for one spectrometer measurement. To further constrain divergence angle, they compared angularly resolved multiple bremsstrahlung measurements to calculation using a hybrid transport code that includes resistivity and magnetic fields. For the electron source, Chen used 2D PIC-calculated information parameterized for a 2D hybrid transport code, [28] while Westover varied the incident electron parameters[29]. Their methods significantly constrain the electron distribution, however simultaneous agreement between bremsstrahlung measurements at multiple angles and modeling using a unique electron input parameter has not been obtained.

We have used a hybrid PIC code, LSP[30], to simulate the transport of fast electrons and generation of bremsstrahlung in a Cu foil by injecting fast electrons. The electron transport and angular bremsstrahlung calculated by the code are benchmarked against a Monte Carlo simulation. It is found that non-normal electron injection angle in a 2D Cartesian geometry is necessary to reproduce the trend of measured bremsstrahlung signals at two angular spectrometer positions in the experiment. The simulated bremsstrahlung is simultaneously fit to the two angularly resolved measurements to determine a slope temperature and a divergence of injected fast electrons.

2. Experiment

The experiment was carried out at the NTF using the 50 TW Leopard laser[31]. The targets used in this experiment were 100 μm thick Cu foils with a surface area of 1x1 mm^2 mounted on a thin glass stalk. Figure 1(a) shows a schematic of the experimental setup. The Leopard laser produces pulses with 15J energy in 0.35 ps pulse duration at a central wavelength of 1057 nm. The beam was tightly focused with a f/1.5 off-axis parabolic mirror onto the Cu target at an incident angle of 30° with an S-polarization. The bremsstrahlung X rays were measured at 22˚ and 40˚ from the laser axis with two differential filter stack spectrometers with a spectral range from 10 to 800 keV[23]. The escaped electrons were measured directly with an absolutely calibrated magnet-based electron spectrometer[32] fielded along the laser axis. Figure 1(b) and (c) shows measured escaped electron spectrum and both bremsstrahlung spectrometer signals for a bare 100 μm Cu foil. The slope of the electrons fit with an exponential function is estimated to be 1.1 ± 0.15 MeV. In the bremsstrahlung spectrometer, metal filters and image plate (IP) detectors are alternated so that the depth of the IP layers corresponds to increasing photon energies. The bremsstrahlung signals observed at the two angular positions show an anisotropic trend as the angle from target normal is deviated. The signal at 40˚ is approximately 1.6 times lower than that at 22˚. The error bars in the experimental data are estimated from quadrature addition of the standard deviation, the gradient of the cannon signal, and a 3% scanner response variation arising from the IPs[26].

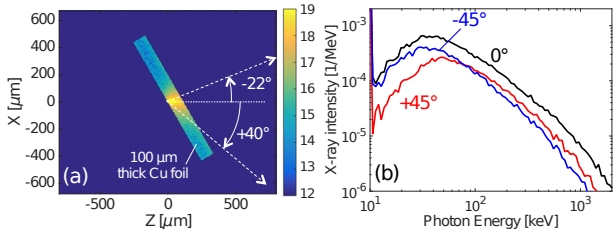

Figure 2 (a) 2D XZ LSP simulation of a 100 μm Cu foil tilted by 30°. Fast electrons are injected in +Z direction at Z=X=0. (b) Bremsstrahlung spectra along the injection axis at 0˚ and at ±45˚.

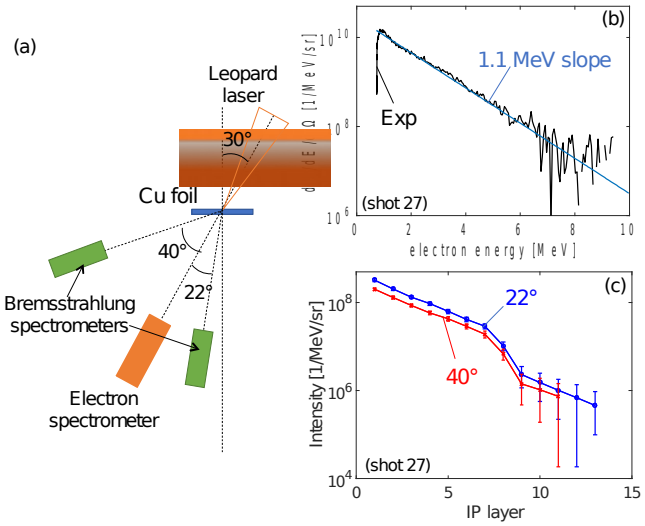

Figure 1: (a) A schematic of the laser and diagnostic layout. (b) Measured escaped electron energy spectrum for the 100 μm Cu foil, with a best slope fitting of 1.1 MeV. (c) The resulting bremsstrahlung spectrometer signals at 22° and 40°.

3. LSP simulations

3.1 Modeling of angularly resolved bremsstrahlung for the Leopard laser experiment

Bremsstrahlung at the experimental detector positions is modeled with a hybrid PIC code LSP in a 2D XZ geometry. Benchmarking of electron stopping and bremsstrahlung production models in LSP against a Monte Carlo code is performed and presented in Appendix A. Figure 2(a) shows the simulation geometry of a tilted Cu foil by 30˚. An electron beam having a 20 μm spot is injected at Z=0 in +Z direction. Simulations presented below include developments of self-generated fields during the electron transport. Simulation parameters varied are fast electron energy spectrum characterized by an exponential slope (slope temperature, T_{hot}), divergence half-angle (θ) and total injected energy (E). Changes in the total injected energy only vary the total electron number. The electron divergence is included using a Gaussian function. The simulation box size is 1.6 mm x 1.6 mm with a cell size of 10 μm in each dimension, and all simulations are run up to 20 ps. The time step is determined in the code by using a courant multiplier of 0.5.

Figure 2 shows results of photon generations within the Cu foil and angular bremsstrahlung spectra for the injection of an electron beam of T_{hot} of 1.0 MeV, θ =15˚ and E = 0.3 J. The emission distribution shown in Fig. 2(a) represents photons between 10 keV and 50 keV. Each photon born in the Cu foil is transported through the foil and angularly resolved bremsstrahlung spectra are calculated. Fig. 2(b) shows simulated bremsstrahlung spectra at 0˚, +45˚ and -45˚ directions with respect to the electron injection direction (0˚) in clockwise and counterclockwise, respectively. While the x-ray intensity along the injection axis is the highest, the x-ray spectra at ±45˚ show an anisotropic trend. In particular, the spectra below ~100 keV are significantly different between ±45˚. These anisotropic x-ray spectra cannot be simulated in axisymmetric 2D cylindrical geometry. Simulations in 2D Cartesian coordinate, therefore, are required to model bremsstrahlung measurements at multiple angular positions in experiments with a non-normal incident angle. To clarify the experimental detector positions in the simulation geometry, the one close to the injection axis is at -22˚ and the other one is at +40˚.

3.2 Sensitivity of simulated bremsstrahlung signals on divergence angle, total injected energy and energy spectrum

To compare the simulations to the measurement, the simulated bremsstrahlung spectrum is post-processed using a spectrometer response function to calculate corresponding signal doses in the bremsstrahlung spectrometers. In our previous study[22], the spectrometer signals were converted to a photon energy spectrum by taking differences in signals between consecutive layers for comparing to a PIC simulation. Since this analysis enhances errors due to low photon signals, particularly at high photon energies, the simulation only broadly agrees with the experiment. In this section, sensitivities of the simulated detector signals on inputs of θ, T_{hot} and total injected energy are presented to later directly compare to the experiments with the intrinsic experimental errors.

Figure 3 shows simulated spectrometer signals at the -22˚ and +40˚ detector positions for θ of 1˚, 15˚ and 30˚ with T_{hot} = 1.1 MeV. The

injected energy is fixed to 0.3 J. As the divergence angle increases the anisotropic trend between the signals decreases. The two spectrometer signals overlap with θ = ~30˚, which does not agree with the measurement shown in Fig. 1(c). The dependence of the signal ratio on the divergence holds with different electron energy spectra. The simulation results suggest that bremsstrahlung measurements at multiple angular positions could be used to determine the divergence of the fast electrons. Here, the divergence angle in the simulation is qualitatively determined to be less than ~ 30˚ to match the experiment.

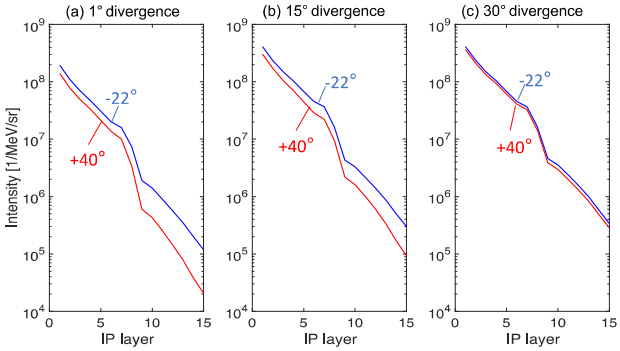

Figure 3: Simulated bremsstrahlung spectrometer signals for (a) θ = 1˚, (b) 15˚ and (c) 30˚.

Figure 4(a-c) show changes in the input electron spectra, bremsstrahlung spectra and the resulting spectrometer signals with T_{hot} of 0.5, 1.0 and 1.5 MeV for θ = 15˚ and E=0.3 J. Since the total injected energy (electron number) is fixed, the number of electrons at low energies (< ~ 1 MeV) is higher with T_{hot} = 0.5 MeV than with 1.5 MeV, whereas the trend is reversed at higher photon energies. The changes in the electron spectra are clearly seen in the calculated bremsstrahlung as well as the simulated spectrometer signals as shown in Fig. 4(b) and (c), demonstrating that an input electron energy spectrum can be determined by fitting the bremsstrahlung spectrometer signals with various T_{hot}.

Fig.4 (d) shows dependence of simulated spectrometer signals on injected energies (0.5, 1.0 and 1.5 J) using T_{hot} = 1.0 MeV and θ = 15˚. The signal strength is linearly lowered as the total injected energies decrease. In fact, the dose signals divided by the corresponding total injected energy agree with each other. Thus, in this study, the measurements and simulated signals are compared with a grid of simulations with various T_{hot} and θ in an arbitrary unit to neglect the dependence of the total injected energy as shown below.

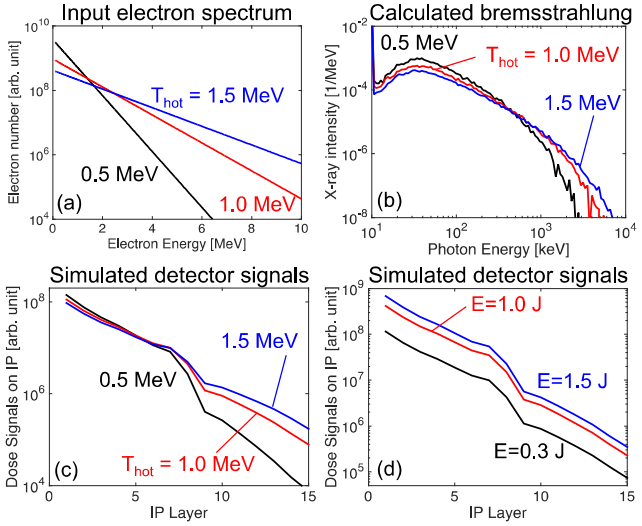

Figure 4 (a) Input electron spectra for T_{hot} = 0.5, 1.0 and 1.5 MeV with a constant energy of E=0.3 J. (b) Simulated bremsstrahlung spectra for varying T_{hot} at -22˚. (b) Simulated spectrometer signal for varying T_{hot}. (c) Simulated spectrometer signal for varying injected energies.

4. Results and Discussion

A series of simulations performed with the parameter ranges of 0.5 ≤ T_{hot} ≤ 1.5 MeV and 1˚ ≤ θ ≤ 40˚ is compared to the measurements. The simulated spectrometer signal at the 7th layer is unchanged for a constant injected energy [see Fig.4 (c)]. Thus, the simulated and experimental spectrometer signals at +40˚ are normalized to the signal at the 7th layer, and the same normalization factors are applied for the signals at -22˚ so that the relative intensities between two spectrometer signals are maintained. This is done to compare the simulation and experiment in an arbitrary unit to ignore the dependency on the conversion efficiency of laser to fast electrons.

Figure 5 shows comparisons of the experimental signals with simulated spectrometer signals and a χ^2 map for simultaneous fits to the two measurements at -22˚ and +40˚. A best fit is found for T_{hot} of 1.0 MeV and θ of 15˚ from the fit. As shown in Fig.5 (a) and (b), the simulated signals for T_{hot} = 0.5 and 1.5 MeV clearly bound the

experimental data. The measured signals at -22° agree with a colder $T_{hot} \leq \sim 1.0$ MeV, while the signals at +40° are close to the simulations between 1.0 and 1.5 MeV. Changes in the divergence angle have little effect on the simulated spectra for $\theta \leq 15°$. In Fig.5 (c) and (d), the measurement and the simulated signals are in reasonable agreement with LSP for $5° \leq \theta \leq 15°$. For a large divergence angle at 30°, the simulated signals deviate from the measurement, particularly for the one close to the injection axis (-22°). Fig.5 (e) displays a linearly interpolated χ^2 map obtained from the fitting. The χ^2 map and a contour of twice of the minimum value (red dotted line) shows the ranges of $T_{hot} = 1.1 \pm 0.3$ MeV and $\theta = 15° \pm 8°$. A slight deviation observed between the measurement and simulations even with the best-fit parameters [e.g., the 1st data point in Fig.5 (b)] could be due to the target misalignment (rotation angle). Similar parameter ranges are inferred at different injected energies.

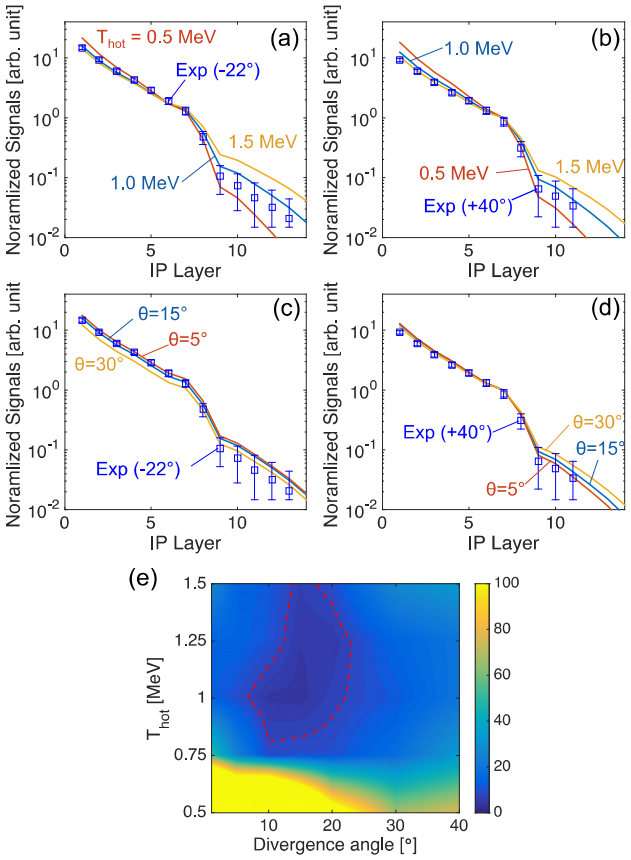

Figure 5 Comparisons of simulated spectrometer signals with (a) –22° and (b) +40° spectrometers with T_{hot} of 0.5, 1.0 and 1.5 MeV for $\theta = 15°$. Comparisons of simulated signals with (c) –22° and (d) +40° spectrometers with $\theta = 5°$, 15° and 30° for $T_{hot} = 1.0$ MeV. (e) Chi-squared fitting of both bremsstrahlung spectrometers simultaneously with the simulated signals. The dotted red line indicates twice the minimum χ^2 value

The electron energy spectrum inferred from the fit to the two bremsstrahlung spectrometer signals agrees with the slope temperature observed in the direct electron measurement shown in Fig. 1(b). This is strong experimental evidence that the bremsstrahlung is predominantly produced by the first pass of MeV electrons, which is predicted by a PIC simulation in our previous work[22]. This is further supported by the fact that the divergence angle of 15° ± 8° from the fit is consistent with the bremsstrahlung confined half angle estimated from $1/\gamma$ (γ =3.18 for 1.1 MeV and θ = 18°), and much narrower than the classical ejection angle of an isolated electron from a laser beam in an underdense plasma ($\theta = \tan^{-1}\left(2/(\gamma-1)\right)^{0.5}$, θ = 44°) [33]. The latter angle is a spread of forward-going electrons in the preplasma at the laser interaction region. The fast electron divergence angle deduced from bremsstrahlung measurements, therefore, is likely an angle of electrons entering the target, which is different from the electron divergence at the generation region.

Understanding the fast electron source is important to accurately determine x-ray spectra and source sizes of fast electron-based x-ray radiation. Recirculation of fast electrons due to sheath potentials could alter bremsstrahlung spectra. However, the effect is minimal in this study as shown in Appendix B. The first pass of the high-energy electrons produces a burst of short-duration, bright x-ray source, while X rays produced by the electron recirculation are much less intense and lasts long over tens of picoseconds. For x-ray radiography with broadband spectrum, the former dominant signal can be used to form the image of an object, whereas the latter long-duration X rays add noises to the image. Using the LSP code, studies of time-dependent fast-electron-produced X rays and effect of sheath fields on target types are currently underway for optimization of broadband x-ray sources.

Bremsstrahlung measurements at multiple angular positions along with measurement of escaping electrons could be a suite of single-shot diagnostics to better constrain electron characteristics produced by high energy short-pulse lasers. In the present study, the electron energy spectrum with a single slope temperature is adequate to fit the data. For higher laser energies, inclusion of a second non-thermal component in the energy spectrum is likely necessary in modeling. In 100J class TITAN and LULI experiments, a two-temperature spectrum (T_{hot1} and T_{hot2}, $T_{hot2} > T_{hot1}$) is required for hybrid PIC simulations to match Kα and coherent transition radiation[35] measurements (for instance, T_{hot1} = 300 keV and T_{hot2} = 7 MeV in a TITAN experiment[36]) An electron measurement provides information on the higher energy component, T_{hot2}, while multiple bremsstrahlung measurements could constrain T_{hot1} and divergence angle in a fit. Furthermore, a hybrid transport simulation in 3D Cartesian geometry could constrain the injected electron energy by comparing absolutely calibrated bremsstrahlung measurements, providing information on the conversion efficiency of laser to hot electrons in addition to divergence angle and slope temperature of energy distribution.

5. Conclusions

Modeling of angularly resolved bremsstrahlung measurements with a hybrid PIC code LSP for determining fast electron energy spectrum and divergence angle is presented. LSP simulations in a 2D Cartesian coordinate with a non-normal injection angle matching the experimental laser incident angle is required to reproduce the trend of the measured bremsstrahlung at multiple angular positions. From simultaneous fitting of two bremsstrahlung signals, the range of slope temperatures and divergence angles are inferred to be 1.1 ± 0.3 MeV and 15° ± 8°. The T_{hot} inferred from the analysis of the bremsstrahlung and the escaped electron measurement agrees well, suggesting that the high energy fast electrons propagating in the first pass are mainly responsible for producing the bremsstrahlung measured.

Acknowledgement

The authors would like to acknowledge Dr. P. Wiewior and O. Chalyy for their support of the Leopard laser operations, A. Astanovitskiy, O. Dmitriev, V. Nalajala and V. Davis for conducting the experiment, and the NTF management for allocation of the laser time. H.S. would like to thank Dr. C. D. Chen for his suggestions on the code benchmarking. This work was supported by the National Science Foundation under Grant No. 1707357. Y.S. was supported by DOE/OFES under Contract No. DE-SC0008827. This collaborative work was partially supported under the auspices of the US Department of Energy by Lawrence Livermore National Laboratory under Contracts No. DE-AC52-07NA27344 and No. DEFG-02-05ER54834 (ACE).

Appendix A: Benchmarking of LSP against Monte Carlo code

Simulations with a non-normal beam injection must be performed in 2D or 3D Cartesian coordinates. Since most simulations using LSP have been performed in 2D cylindrical geometry[37,38,39], electron stopping and bremsstrahlung production models in a 2D XZ Cartesian coordinate are compared to a Monte Carlo code.

Benchmarking of the fast electron transport package and the angular bremsstrahlung spectra in LSP is performed against a Monte Carlo code EGS5[40] incorporated in Particle and Heavy Ion Transport code System (PHITS) (version 3.02)[41]. In PHITS, the electron and photon transport are calculated using EGS5. The collisional model in LSP is based on continuous-slowing-down approximation (CSDA) range for fast electrons taking into account both binary collisions with plasma ions and electrons as well as collective plasma effects such as excitation of plasma waves[42,43,44]. In LSP, Kα and bremsstrahlung are modeled using the Integrated Tiger Series (ITS) Monte-Carlo code[45] for photon generations. Angularly and spectrally resolved photon information outside the target is calculated by transporting the photons through the path length in a cold material.

A test simulation is performed to model the collisional stopping range of collimated 1 MeV monoenergetic electrons injected in a 1 mm thick solid Cu foil. A LSP simulation is performed in the 2D Cartesian coordinate,

while PHITS is used in the 3D Cartesian geometry. The electric and magnetic fields generated by the electrons are turned off in LSP to emulate the physics in the Monte Carlo code. In Figure 6 (a), a beam of the electrons are injected at X = Z = 0 μm in the +Z direction. As the electrons collisionally slow down in the foil, the interaction between the electron and the Cu atoms produces characteristic Kα emission that represents the spatial distribution of the propagating electrons in the scattering and the energy loss mechanisms. Figure 6 (a) shows a 2D Kα emission distribution from the Cu foil. The collimated electron beam not only slows down in the forward direction, but also is strongly scattered both in the side and backward directions. A similar spatial distribution of the Kα map is obtained in the XZ plane of the 3D PHITS calculation. Fig. 6 (b) compares lineouts of the LSP- and PHITS-calculated Kα spatial distribution at X = 0. The result is in good agreement between the two codes, suggesting that LSP in the 2D Cartesian coordinate can reproduce the electron transport in cold solid Cu targets.

To compare the resulting angular bremsstrahlung spectra exiting the foil, the target geometry is changed to a 100 μm thick, and 600 μm wide Cu foil with the same 1 MeV monoenergetic injection at the normal incidence. Fig. 6(c) shows spatial distribution of photons above 10 keV generated within the Cu foil. After taking the x-ray attenuation by the foil into account using cold opacity, spectrally resolved x-ray signals are collected with 5° angular bins from the forward direction at 0° (+Z direction) to 180° (-Z direction). The x-ray signals are symmetric between 0° ~ 180° and 180° ~ 360° since the electrons are injected at normal to the foil. Fig. 6(d) compares angularly resolved bremsstrahlung calculated from LSP and PHITS at 25°, 45° and 60°. The 45° and 60° signals were divided by 10 and 100 respectively to easily view the agreement between the calculations. The simulated x-ray spectra including the Kα yields agree well at each angle. This agreement holds when the injection of the electrons is changed from normal to a 30° incident angle.

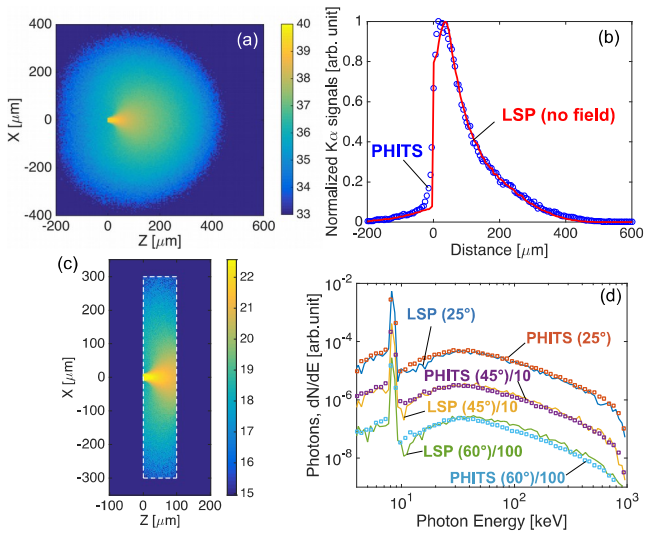

Figure 6 (a) Contour of 1 MeV electron-induced Kα emission within a 1 mm thick Cu foil. (b) A comparison of the Kα emission lineout along the injection axis. (c) Spatial distribution of x-rays produced within a 100 μm Cu foil. (d) Angular bremsstrahlung spectra from LSP and PHITS. The spectra at 45° and 60° are divided by 10 and 100, respectively for clarification.

Appendix B: Effect of sheath fields on bremsstrahlung

Figure 7 (a) and (b) show electron particle trajectories with 3 MeV energies in the simulations with fields off and on. The simulations are performed with a slope temperature of 1.1 MeV and the divergence angle of 15°. With fields off, the MeV electrons ballistically travel through and exit from the foil. In contrast to the no field case, a sheath potential is formed on the target surfaces from the charge separation resulting from the very high energy electrons exiting the foil, which confines the lower energy electrons around the target. Particularly in this titled target, the electrons are guided along the foil surface to the +60° direction. As reported by Cottrill et al[46], the surface sheath fields not only change the direction of fast electrons, but also enhance the number of interaction between the electrons and the foil, which consequently produces more Kα and bremsstrahlung x-rays.

Fig. 7(c) and (d) show time-integrated x-ray spectra for the cases with field developments off and on for the total injected energy of 0.3 J and 1 J. The effect of the sheath field on the

bremsstrahlung spectra is negligible with 0.3 J. However, the difference between the two spectra with fields on and off becomes larger with increasing the total energy injected. In this case, the x-ray intensity peaking at the photon energy of 40~50 keV is ~ 1.3 times higher than that with the fields off. The x-ray signals above 200 keV are unchanged by the field effect. This result indicates that modeling of bremsstrahlung with electron and photon transport codes that do not model self-consistent sheath fields could lead to overestimation of laser-to-electron coupling efficiency.

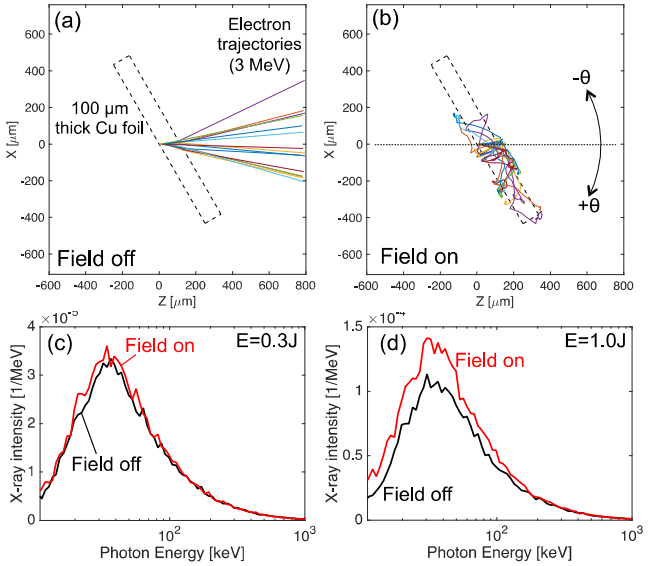

Figure 7 (a) Electron particle trajectories for 15 particles with 3 MeV energies for an injection with self-consistent fields turned off. (b) with the fields turned on, (c), (d) Bremsstrahlung spectra for the cases with fields off and on for energies of 0.3 J and 1.0 J respectively.

1 H.-S. Park, B. R. Maddox, E. Giraldez, S.P. Hatchett, L.T. Hudson, N. Izumi, M. H. Key, S. Le Pape, A.J. Mackinnon, A. G. MacPhee, P. K. Patel, T. W. Phillips, B. A. Remington, J. F. Seely, R. Tommasini, R. Town, J. Workman, and E. Brambrink, Phys. Plasmas 13, 056309 (2006).
2 R. D. Edwards, M.A. Sinclair, T.J. Goldsack, K. Krushelnick, F.N. Beg, E.L. Clark, A.E. Dangor, Z. Najmudin, M. Tatarakis, B. Walton, M. Zepf, K.W.D. Ledingham, I. Spencer, P.A. Norreys, R.J. Clarke, R. Kodama, Y. Toyama, and M. Tampo, Appl. Phys. Lett. 80, 2129 (2002).
3 E. L. Clark, K. Krushelnick, J. R. Davies, M. Zepf, M. Tatarakis, F. N. Beg, A. Machacek, P. A. Norreys, M. I. K. Santala, I. Watts and A. E. Dangor, Phys. Rev. Lett. 84, 670 (2000).
4 S. C. Wilks, A. B. Langdon, T. E. Cowen, M. Roth, M. Singh, S. Hatchett, M. H. Key, D. Pennington, A. MacKinnon, and R. A. Snavely, Phys. Plasmas 8, 542 (2001).
5 A. P. L. Robinson, M. Zepf, S. Kar, R. G. Evans, and C. Bellei, New. J. Phys. 10, 013021 (2008).
6 M. Storm, S. Jiang, D. Wertepny, C. Orban, J. Morrisson, C. Willis, E. McCary, P. Belancourt, J. Snyder, E. Chowdhury, W. Bang, E. Gaul, G. Dyer, T. Ditmire, R. R. Freeman, and K. Akli, Phys. Plasmas 20, 053106 (2013).
7 M. Tabak, J. Hammer, M. E. Glinsky, W. L. Kruer, S. C. Wilks, J. Wood- worth, E. M. Campbell, M. D. Perry, and R. J. Mason, Phys. Plasmas 1, 1626 (1994).
8 R. Kodama, P. A. Norreys, K. Mima, A. E. Dangor, R. G. Evans, H. Fujita, Y. Kitagawa, K. Krushelnick, T. Miyakoshi, N. Miyanaga et al., Nature 412, 798 (2001).
9 L. Pandola, C. Andenna, B. Caccia, Nuc. Instrum. and Methods in Phys. Research B 350, 41-48 (2015).
10 R. Tommasini, S.P. Hatchett, D.S. Hey, C. Iglesias, N. Izumi, J. A. Koch, O.L. Landen, A. J. MacKinnon, C. Sorce, J. A. Delettrez, V.Y. Glebov, T.C. Sangster, and C. Stoeckl, Phys. Plasmas 18, 056309 (2011).
11 R. Tommasini, C. Bailey, D.K. Bradley, M. Bowers, H. Chen, J.M. Di Nicola, P. Di Nicola, G. Gururangan, G.N. Hall, C.M. Hardy, D. Hargrove, M. Hermann, M. Hohenberger, J.P. Holder, W. Hsing, N. Izumi, D. Kalantar, S. Khan, J. Kroll, O.L. Landen, J. Lawson, D. Martinez, N. Masters, J.R. Nafziger, S.R. Nagel, A. Nikroo, J. Okui, D. Palmer, R. Sigurdsson, S. Vonhof, R.J. Wallace, and T. Zobrist, Phys. Plasmas **24**, 053104 (2017).
12 H. Sawada, T. Daykin, B. Bauer and F. Beg, APS Division of Plasma Physics Meeting 2017, abstract id. NO6.002
13 P. Norreys, D. Batani, S. Baton, F.N. Beg, R. Kodama, P.M. Nilson, P. Patel, F. Pérez, J.J. Santos, R.H.H. Scott, V.T. Tikhonchuk, M. Wei, and J. Zhang, Nucl. Fusion **54**, 054004 (2014).
14 M. H. Key, M .D. Cable, T. E. Cowan, K. G. Estabrook, B. A. Hammel, S. P. Hatchett, E. A. Henry, D. E. Hinkel, J. D. Kilkenny, J. A. Koch et al., Phys. Plasmas 5, 1996 (1998).
15 C. Courtois, A. C. L. Fontaine, O. Landoas, G. Lidove, V. Meot, P. Morel, R. Nuter, E. Lefebvre, A. Boscheron, J. Grenier et al., Phys. Plasmas 16, 013105 (2009).
16 S. P. Hatchett, C. G. Brown, T. E. Cowan, E. A. Henry, J. S. Johnson, M. H. Key, J. A. Koch, A. B. Langdon, B. F. Lasinski, R. W. Lee et al., Phys. Plasmas 7, 2076-82 (2000).
17 R. H. H. Scott, E. L. Clark, F. Perez, M. J. V. Streeter, J. R. Davies, H. P. Schlenvoigt, J. J. Santos, S. Hulin, K. L. Lancaster, S. D. Baton, S. J. Rose, and P. A. Norreys, Rev. Sci. Instrum. 84, 083505 (2013).
18 A. L. Meadowcroft, R. D. Edwards, IEEE Trans. Plasma Sci. 40, 1992-2001 (2012).
19 J. Galy, M. Maucec, D. J. Hamilton, R. Edwards, J. Magill, New J. Phys. 9, 23 (2007).
20 C. Zulick, B. Hou, F. Dollar, A. Maksimchuk, J. Nees, A. G. R. Thomas, Z. Zhao, and K. Krushelnick, New J. Phys. 15, 123038 (2013).
21 K. B. Wharton, S. P. Hatchett, S. C. Wilks, M. H. Key, J. D. Moody, V. Yanovsky, A. A. Offenberger, B. A. Hammel, M. D. Perry, and C. Joshi, Phys. Rev. Lett. 81, 822 (1998).
22 H. Sawada, Y. Sentoku, A. Bass, B. Griffin, R. Pandit, F. N. Beg, H. Chen, H. McLean, A. J. Link, P. K. Patel, and Y. Ping, J. Phys. B: At. Mol. Opt. Phys. 48, 224008 (2015).
23 C. D. Chen, J. A. King, M. H. Key, K. U. Akli, F.N. Beg, H. Chen, R.R. Freeman, A. Link, A.J. Mackinnon, A.G. MacPhee, P. K. Patel, M. Porkolab, R.B. Stephens, and L. D. Van Woerkom, Rev. Sci. Instrum. 79, 10E305 (2008).
24 Y. J. Rhee, S. M. Nam, J. Peebles, H. Sawada, M. Wei, X. Vaisseau, T. Sasaki, L. Giuffrida, S. Hulin, B. Vauzour, J. J. Santos, D. Batani, H. S. McLean, P. K. Patel, Y. T. Li, D. W. Yuan, K. Zhang, J. Y. Zhong, C. B. Fu, N. Hua, K. Li, Y. Zhang, J. Q. Zhu, I. J. Kim, J. H. Jeon, T.M. Jeong, I. W. Choi, H.W. Lee, J. H. Sung, S. K. Lee, and C. H. Nam, Laser Part. Beams 96, 1 (2016).

25 C. Courtois, R. Edwards, A. Compant La Fontaine, C. Aedy, S. Bazzoli, J. L. Bourgade, J. Gazave, J. M. Lagrange, O. Landoas, L. Le Dain, D. Mastrosimone, N. Pichoff, G. Pien, and C. Stoeckl, Phys. Plasmas **20**, 083114 (2013).
26 C. D. Chen, P. K. Patel, D. S. Hey, A. J. Mackinnon, M. H. Key, K. U. Akli, T. Bartel, F. N. Beg, S. Chawala, H. Chen et al., Phys. Plasmas 16, 082705 (2009).
27 B. Westover, C. D. Chen, P. K. Patel, M. H. Key, H. McLean, R. Stephens, and F. N. Beg, Phys. Plasmas **18**, 063101 (2011).
28 C. D. Chen, A. J. Kemp, F. Pérez, A. Link, F. N. Beg, S. Chawla, M. H. Key, H. McLean, A. Morace, Y. Ping, A. Sorokovikova, R. B. Stephens, M. Streeter, B. Westover, and P. K. Patel, Phys. Plasmas **20**, 052703 (2013).
29 B. Westover, C. D. Chen, P. K. Patel, H. McLean, and F. N. Beg, Phys. Plasmas **21**, 031212 (2014).
30 D. Welch, D. Rose, B. Oliver, and R. Clark, Nucl. Instrum. Methods Phys. Res. A 464, 134 (2001).
31 P.P. Wiewior, V. V Ivanov, and O. Chalyy, J. Phys. Conf. Ser. **244**, 032013 (2010).
32 H. Chen, P. K. Patel, D. F. Price, B. K. Young, P. T. Springer, R. Berry, R. Booth, C. Bruns and D. Nelson, Rev. Sci. Instrum. **74,** 1551 (2003).
33 C. I. Moore, J. P. Knauer, and D. D. Meyerhofer, Phys. Rev. Lett. 74, 2439 (1995).
34 H. Sawada, D. P. Higginson, A. Link, T. Ma, S. C. Wilks, H. S. McLean, F. Pérez, P. K. Patel, and F. N. Beg, Phys. Plasmas 19, 103108 (2012).
35 J. J. Santos, A. Debayle, P. Nicolaï, V. Tikhonchuk, M. Manclossi, D. Batani, A. Guemnie-Tafo, J. Faure, V. Malka, and J. J. Honrubia, Eur. Phys. J. Spec. Top. 175, 71 (2009).
36 T. Ma, H. Sawada, P. K. Patel, C. D. Chen, L. Divol, D. P. Higginson, A. J. Kemp, M. H. Key, D. J. Larson, S. Le Pape, A. Link, A. G. MacPhee, H. S. McLean, Y. Ping, R. B. Stephens, S. C. Wilks, and F. N. Beg, Phys. Rev. Lett. 108, 115004 (2012).
37 R. P. J. Town, C. Chen, L. A. Cottrill, M. H. Key, W. L. Kruer, A. B. Langdon, B. F. Lasinski, R. A. Snavely, C. H. Still, M. Tabak, D. R. Welch, and S. C. Wilks, Nucl. Instruments Methods Phys. Res. Sect. A Accel. Spectrometers, Detect. Assoc. Equip. 544, 61 (2005).
38 A. Link, R.R. Freeman, D.W. Schumacher, and L.D. Van Woerkom, Phys. Plasmas 18, 053107 (2011).
39 A. A. Solodov, K. S. Anderson, R. Betti, V. Gotcheva, J. Myatt, J. A. Delettrez, S. Skupsky, W. Theobald, and C. Stoeckl, Phys. Plasmas **16**, 056309 (2009).
40 Hirayama H, Namito Y, Bielajew AF, Wilderman SJ, and Nelson WR, The EGS5 code system. Menlo Park, USA and Tsukuba, Japan: SLAC National Accelerator Laboratory and High Energy Accelerator Research Organization; 2005. (SLAC-R-730 and KEK Report 2005-8).
41 T. Sato, Y. Iwamoto, S. Hashimoto, T. Ogawa, T. Furuta, S. Abe, T. Kai, P.-E. Tsai, N. Matsuda, H. Iwase, N. Shigyo, L. Sihver, and K. Niita, J. Nucl. Sci. Technol. **55**, 684 (2018).
42 A. A. Solodov and R. Betti, Physics of Plasmas 15, 042707 (2008).
43 S. Atzeni, A. Schiavi, and J. R. Davies, Plasma Physics and Controlled Fusion 51, 015016 (2009).
44 H. W. Lewis, Physical Review 78, 526 (1950).
45 J. A. Halbleib, R. P. Kensek, G. D. Valdez, S. M. Seltzer, M. J. Berger, IEEE Transactions on Nuclear Science 39, 1025 (1992).
46 L. A. Cottrill, A. Kemp, M. Tabak, R. P. J. Town, Nucl. Fusion 50, 095002 (2010).